

Numerical study of tidal circulation and nonlinear dynamics in Lunenburg Bay, Nova Scotia

Jinyu Sheng and Liang Wang

Department of Oceanography, Dalhousie University, Halifax, Nova Scotia, Canada

Received 30 March 2004; revised 20 July 2004; accepted 3 September 2004; published 30 October 2004.

[1] A three-dimensional ocean circulation model is used to study the barotropic tidal circulation and nonlinear tidal dynamics in Lunenburg Bay, Nova Scotia. The model performance is first assessed using the observed bottom pressures and currents made in Septembers of 1991 and 2003. The model results reproduce reasonably well the observed tidal circulation in the study region. The simulated tidal circulation is dominated by the semidiurnal (M_2) tide and an intense jet-like flow through a narrow channel connecting Lunenburg Bay and two shallow coves. To demonstrate the importance of nonlinear tidal dynamics in the region, the first two harmonics of M_2 (i.e., M_4 and M_6) are computed from the model results forced by the M_2 tide at the model open boundaries. Both M_4 and M_6 are relatively large in western Lunenburg Bay and vicinity, indicating the importance of the nonlinear tidal dynamics over these areas. To quantify the role of various nonlinear terms in generating the intense jet and associated residual flows in the region of the jet, both transient and tidally averaged (time mean) momentum equations are examined. The transient and time mean momentum balances demonstrate that the nonlinear interaction of the tidal currents with local bathymetry is balanced primarily by the horizontal pressure gradients, momentum advection, and dissipation. The Coriolis effect plays a minor role in the study region. *INDEX TERMS*: 4560 Oceanography: Physical: Surface waves and tides (1255); 4528 Oceanography: Physical: Fronts and jets; 4255 Oceanography: General: Numerical modeling; 4223 Oceanography: General: Descriptive and regional oceanography; 4512 Oceanography: Physical: Currents; *KEYWORDS*: tidal circulation, nonlinear dynamics, numerical model

Citation: Sheng, J., and L. Wang (2004), Numerical study of tidal circulation and nonlinear dynamics in Lunenburg Bay, Nova Scotia, *J. Geophys. Res.*, 109, C10018, doi:10.1029/2004JC002404.

1. Introduction

[2] Estuaries and embayments are semienclosed bodies of seawater situated at the interface between land and ocean. The mixing and dispersion in these regions and their exchange with the open ocean are key processes that affect the distribution and transport of pollutants, nutrients, larval stage of some biological species, suspended sediment and other water-borne material [Signell and Butman, 1992]. Better understanding of physical processes at work in these regions is of great importance for successful management of the coastal and marine resources for sustainable use in the future.

[3] Lunenburg Bay (hereinafter LB) is a shallow coastal embayment situated on the south shore of Nova Scotia, with a surface extension of about 8 km by 5 km and water depth of at most 25 m. LB is connected to the Scotian Shelf via Mahone Bay to the southeast, Rose Bay to the southwest, and Upper South Cove (USC) and Lower South Cove (LSC) via a narrow channel known as Corkum's Channel (Figure 1). USC and LSC are each about 3 km long with a

typical water depth of about 3 m. These two coves are linked through a narrow mouth of about 60 m wide. Circulation in LB and two coves is dominated by the semidiurnal tide (M_2), with the typical spring and neap tidal ranges of about 2 m and 1 m, respectively. Because of the hydraulic control of the narrow mouth connecting the two coves, the tidal circulation in USC differs significantly from that in LB and LSC. Previous studies [Thompson *et al.*, 1998] indicates that the amplitude and phase of M_2 in LB are about 0.64 m and 236° , respectively. In comparison, the amplitude and phase of M_2 in USC are respectively about 0.44 m and 277° , which means that the M_2 tide in USC peaks about one and a half hours after it reaches a maximum in LB, with an amplitude deduction of about 31% from LB to USC. Therefore the narrow channel and mouth connecting LB and two coves play a very important role in determining the tidal circulation in LB and two coves.

[4] Various physical and biological measurements were made in LB in the past [Dowd, 1997; Sturley *et al.*, 1993]. A group of physical and biological oceanographers in the early 1990s conducted an interdisciplinary research program to examine physical and biological conditions affecting the scallop dispersal in LB [Grant *et al.*, 1993]. They also examined the flushing mechanisms associated with an

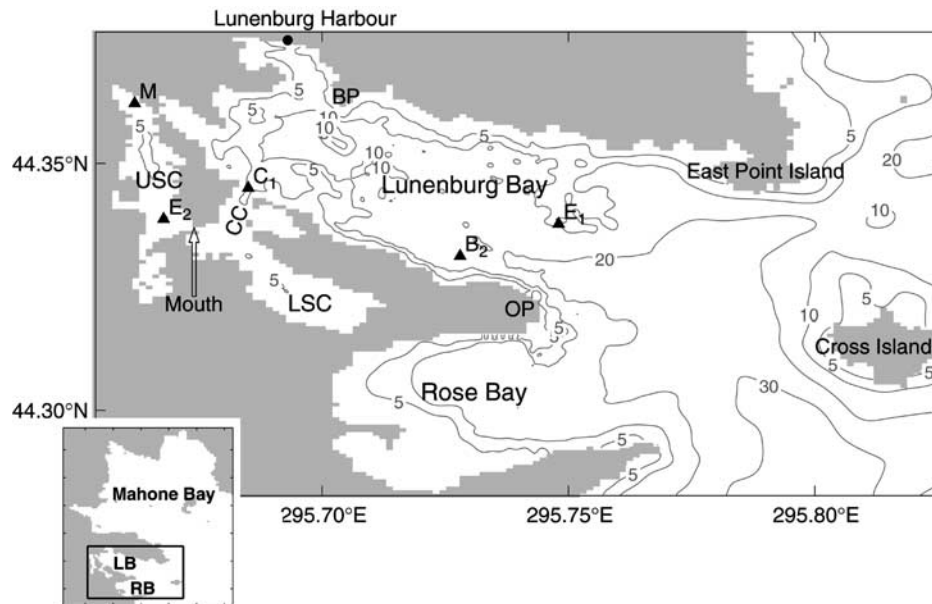


Figure 1. Selected bathymetric features within the model domain. Contours are labeled in meters. Abbreviations are used for Upper South Cove (USC), Lower South Cove (LSC), Corkum's Channel (CC), Battery Point (BP), and Ovens Point (OP). Inset shows a large area that covers Mahone, Lunenburg (LB), and Rose (RB) Bays.

intense tidal jet from LSC to LB during ebb and an asymmetric tidal circulation over western LB. The physical oceanographic variables measured during this program included bottom pressure, currents, temperature and salinity. LB was recently chosen as a testbed for a marine environmental observation and prediction system for the coastal regions of Atlantic Canada, using data assimilative and coupled models guided directly by real-time observations [Safer, 2002]. The coastal circulation model presented in this paper is part of the coastal prediction system currently under development.

[5] *Sturley et al.* [1993] were the first to use a three-dimensional tidal circulation model to study the tidal circulation in LB. Their tidal model generated an intense tidal jet from USC to LB through Corkum's Channel and tidal asymmetry between flooding and ebbing. Using the same model, *Sturley and Bowen* [1996] demonstrated that the tidal circulation in LB is highly nonlinear and advective terms in the momentum equation and the quadratic bottom friction are important in producing the hydraulic control and tidal distortion in the region. *Thompson et al.* [1998] simulated the whirl-like circulation features observed by the synthetic aperture radar over western LB. The nonlinear tidal dynamics in the study region and particularly the nonlinear physical processes associated with the jet-like flow through Corkum's Channel are not, however, well understood.

[6] It should be noted that nonlinear tidal hydrodynamics over coastal embayments and tidal inlets have been studied in the past. The reader is referred to *Parker* [1991] for a comprehensive review of nonlinear tidal interactions in shallow water. *Stommel and Farmer* [1952] developed a conceptual model to describe tidal inlet dynamics and the distinct difference between flood and ebb circulation outside an inlet. *Zimmerman* [1978] and *Robinson* [1981] demonstrated that the tidal flow over topographic features gener-

ates tidal vorticity. They demonstrated that advection of tidal vorticity in opposite directions by the tidal flow is mainly responsible for generating the tidal residual circulation over continental shelf seas. *Chadwick and Largier* [1999] described the tidal exchange at the boundary between a bay and an ocean as a "tidal pumping" process, characterized by an asymmetry between the jet-like nature of the ebb flow and the sink-like nature of the flood flow. *Hench and Luettich* [2003] examined the transient momentum balance of a jet-like flow in a shallow barotropic tidal inlet using a depth-integrated model. Their model results demonstrated that the jet-like flow over the inlet and its vicinity is highly nonlinear, particularly near-maximum ebb or flood tide. Although many aspects of nonlinear tidal dynamics are well known, investigation and quantification of their effects in the region of an intense jet remain to be made.

[7] In this study, we apply a three-dimensional, fine-resolution ocean general circulation model to LB with two main objectives. The first main objective is to validate the model performance by comparing the simulated tidal circulation with the observations made in LB. The second main objective is to examine the tidal circulation and quantify nonlinear tidal dynamics in the study region.

[8] The arrangement of this paper is as follows. The next section briefly discusses the ocean circulation model used in this study. Section 3 assesses the model performance by comparing the simulated tidal circulation with measurements made in LB in Septembers of 1991 and 2003. Section 4 describes the M_2 tidal circulation and associated nonlinear dynamics. Section 5 discusses the jet-like flow through Corkum's Channel and associated transient momentum balance. Section 6 discusses the nonlinear dynamics of the residual flow in the region of the jet. Section 7 examines the model sensitivity to the nonlinear

dynamics retained in the model. The final section is a summary and discussion.

2. Ocean Circulation Model

[9] The tidal circulation model used in this study is the three-dimensional, z level ocean general circulation model known as CANDIE [Sheng *et al.*, 1998]. CANDIE has been successfully applied to various modeling problems on the shelf, including nonlinear dynamics of a density-driven coastal current [Sheng, 2001], tidal circulation in the Gulf of St. Lawrence [Lu *et al.*, 2001a], seasonal circulation over the northwestern Atlantic from northern Labrador to Maine [Sheng *et al.*, 2001], and wind-driven circulation over a stratified coastal embayment [Davidson *et al.*, 2001]. Most recently CANDIE has been applied to the western Caribbean Sea by Sheng and Tang [2003, 2004].

[10] The standard version of CANDIE uses the rigid lid approximation that excludes fast moving surface gravity waves. In studying the internal tide generation over topography, Lu *et al.* [2001b] developed a free surface version of CANDIE by adding a linear free surface to the standard code based on the implicit free surface method suggested by Dukowicz and Smith [1994]. In this study, we use a nonlinear free surface version of CANDIE which retains the nonlinear terms in the continuity equation. Discussions on the governing equations used in the nonlinear free surface version of CANDIE are found in Appendix A.

[11] We run the ocean circulation model in barotropic mode with the model temperature and salinity set to be invariant in time and space. The model domain covers LB, USC and LSC (Figure 1), with a horizontal resolution of 60 m. The model has 23 z levels with a vertical resolution of 1 m, except for 3 m for the top z level and 5.0 m for the last four z levels. Since water depths over USC and LSC are about 3 m or less, there is only one vertical cell over most part of the two coves. The horizontal eddy viscosity coefficient A_m is set to $3 \text{ m}^2 \text{ s}^{-1}$. For the vertical eddy viscosity coefficient K_m in the study region where the bottom boundary layer thickness is limited by the local water depth, we follow Davies [1993] and use

$$K_m = K_o h |\vec{U}_d| \phi(z) \quad (1)$$

where K_o is a dimensionless coefficient set to 3.0×10^{-3} , h is the local water depth, $|\vec{U}_d|$ is the magnitude of the depth mean horizontal velocity vector, and $\phi(z)$ is a prescribed vertical structure function. We follow Davies [1993] and set $\phi(z)$ to be a piecewise linear function, which is equal to unity from surface to $z = -0.8h$ and then decreases linearly to 0.01 at the sea bottom of $z = -h$. A justification of this idealized profile of $\phi(z)$ for simulating the tidal circulation in the coastal region was given by Davies and Jones [1996]. The expression for K_m given in (1) was based on the mixing length theory, in which the vertical eddy viscosity coefficient is proportional to the product of appropriate velocity (v_m) and mixing length (l_m) scales. In this study we follow Bowden [1978] and Davies [1993] and set the velocity scale v_m to $|\vec{U}_d|$ and the mixing length scale l_m to h . It should be noted that K_m in (1) can also be expressed as $K_m = K_1 h u_* \phi(z)$, where $K_1 = K_o C_d^{-1/2}$, C_d is the bottom drag

coefficient, and u_* is the bottom friction velocity estimated by $C_d^{1/2} |\vec{U}_d|$ [Davies, 1993].

[12] At the sea bottom, we use the quadratic bottom friction parameterization defined as:

$$\vec{\tau}_b = \rho_o C_d |\vec{u}_b| \vec{u}_b \quad (2)$$

where $\vec{\tau}_b$ is bottom stress vector and \vec{u}_b is the bottom velocity vector. Recent observations made in Corkum's Channel indicate that the bottom drag coefficient C_d is about 1.0×10^{-2} inside the channel (A. Hay, personal communication, 2004), which is about 3 times larger than the conventional value of 3.0×10^{-3} . Therefore C_d in this study is set to 1.0×10^{-2} in the center of Corkum's Channel, and decreases exponentially to the conventional value of 3.0×10^{-3} with the e -folding distance of 2 km.

[13] At the model lateral closed boundaries, we use the no-slip condition for the horizontal currents. Along the model open boundaries, we use the radiation condition suggested by Davies and Flather [1978]. At the eastern open boundary, for example, we have

$$u_b = u_t + \frac{c}{h} (\eta_b - \eta_t) \quad (3)$$

where u_b is the flow normal to the open boundary, η_b is the model-calculated surface elevation at the open boundary, u_t and η_t are the tidal input of currents and surface elevation at the same open boundary, h is the local water depth, and c can be specified as the external gravity phase speed. Since the free surface version of CANDIE uses the implicit time integration for the external mode, the model time step is not limited by the conventional Courant-Friedrichs-Levy (CFL) stability criterion defined as $\Delta t_C \leq \Delta x / \sqrt{gh}$, where Δx is the model horizontal grid spacing. The maximum water depth is 40 m in the study region (Figure 1). As a result, Δt_C based on the CFL criterion should be less than 3.5 s, which is about 5 times shorter than the model time step of 17 s used in this study. To avoid reflections at the open boundaries, we follow Lu *et al.* [2001b] and set c in (3) to $0.9 \Delta x / \Delta t$.

3. Validation of Barotropic Tidal Simulation in Lunenburg Bay

[14] To validate the model performance, we first compare the simulated tidal circulation with the observations made in the study region during the first 2 weeks of September 1991. Since wind forcing was relatively weak and the sea surface air pressure was relatively steady (not shown) during this period except for that on day 248, the observed bottom pressures (with the time mean removed) shown in Figures 2a and 2b can thus be treated approximately as the adjusted sea level (i.e., the surface elevation with the inverse barometer effect removed). The tidal harmonic analysis using the MATLAB `t_tide` program [Pawlowicz *et al.*, 2002] indicates that tides with 10 constituents (i.e., O_1 , K_1 , M_2 , S_2 , M_3 , M_4 , $2MK_5$, $2SK_5$, M_6 , and M_8) explain about 91% and 87% of the total variance of the observed bottom pressures at E_1 and E_2 , respectively. We define γ_{\min}^2 as the ratio of the variance of the nontidal component to the total observed variance, which denotes the percentage of the observed variance that is not accounted for by the tides. For the observed bottom

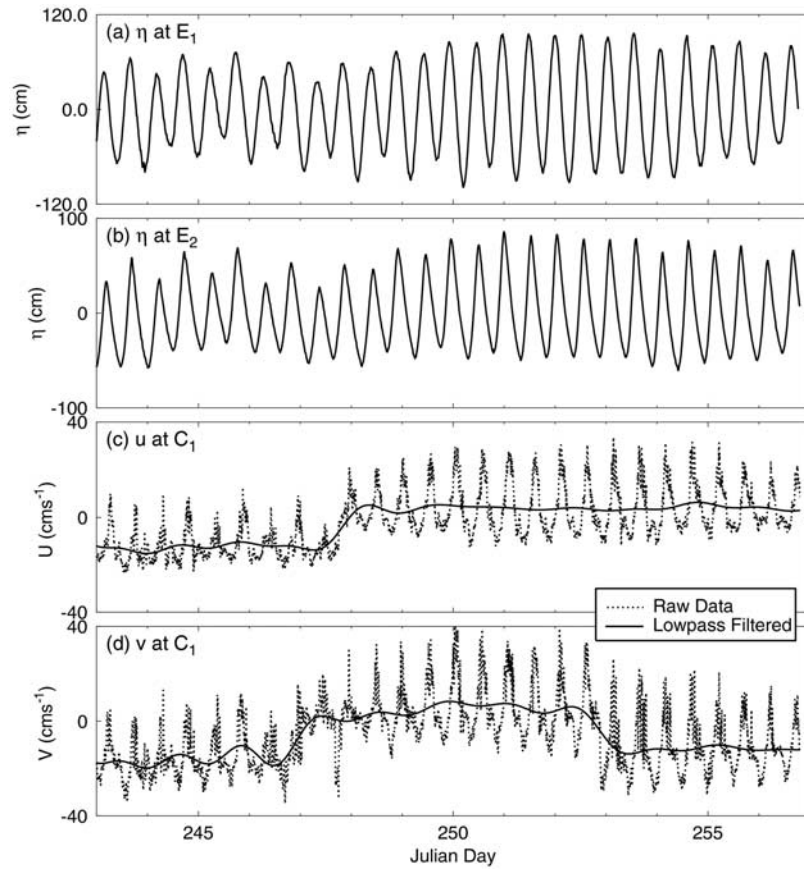


Figure 2. Time series of observed bottom pressures (with time mean removed) at locations (a) E_1 and (b) E_2 , and the (c) eastward and (d) westward components of the near-bottom currents at location C_1 during the first 2 weeks of September 1991.

pressures shown in Figures 2a and 2b the γ_{\min}^2 values are about 0.09 at E_1 and 0.13 at E_2 . The tidal harmonic analysis also confirms that the semidiurnal tide M_2 is the principal constituent at the two locations, which accounts for 88% and 81% of the total observed variance of the bottom pressures at E_1 and E_2 , respectively. However, M_4 and M_6 can only explain 3% or much less of the total bottom pressure at E_1 and E_2 . The luni-solar diurnal tide K_1 accounts for about 2% of the total observed variance at two locations.

[15] In comparison, the observed near-bottom currents at C_1 have not only large tidal components, but also significant subtidal variabilities (Figures 2c and 2d). The main physical processes responsible for this low-frequency variability are not clear. In this study, we only consider the observed currents with the low-frequency variations removed. The dashed lines in Figures 2c and 2d are the low-pass-filtered values with a cutoff period of 27 hours. The harmonic analysis shows that tides with 10 constituents account for about 72% and 62% of the total variance of the low-pass-filtered current measurements at C_1 in the eastward and northward directions (Figures 3c and 3d), respectively. The γ_{\min}^2 values are about 0.28 and 0.38 respectively for the eastward and northward components of the observed currents at C_1 . The M_2 tide accounts for about 65% and 54% of the total variance of the low-pass-filtered currents at C_1 in the eastward and northward directions, respectively. It

should be noted that the observed currents at C_1 have noticeable high-frequency harmonics (the overtones M_4 and M_6 account for about 5% and 0.5% of the total observed variance at C_1) and the observed surface elevations at E_2 have relatively large ebb-flood asymmetry, indicating the importance of the nonlinear tidal dynamics over Corkum's Channel and its vicinity (see sections 4–7 for more discussion).

[16] To simulate the tidal circulation in LB during this period, we drive the high-resolution coastal circulation model with the tidal forcing specified in terms of u_t and η_t in (3) at the model open boundaries. Since there were no direct measurements of u_t and η_t at the model open boundaries during this period, we use the sea level tidal prediction at Lunenburg Harbour (η_h^c) provided by the Canadian Hydrographic Service (CHS) to infer the tidal forcing at the open boundaries. We assume that η_t is spatially uniform along the open boundaries for simplicity. We also follow *Thompson et al.* [1998] and assume u_t in (3) is equal to zero. Both assumptions, however, particularly the latter one, could introduce certain errors in numerical simulations that deserves a further study.

[17] We determine η_t from η_h^c on the basis of the following ad hoc approach. We first integrate the coastal circulation model by setting η_t to η_h^c . We then calculate the transfer function (i.e., differences in magnitude and phase) between the model-calculated (η_h^m) and CHS predicted (η_h^c) surface

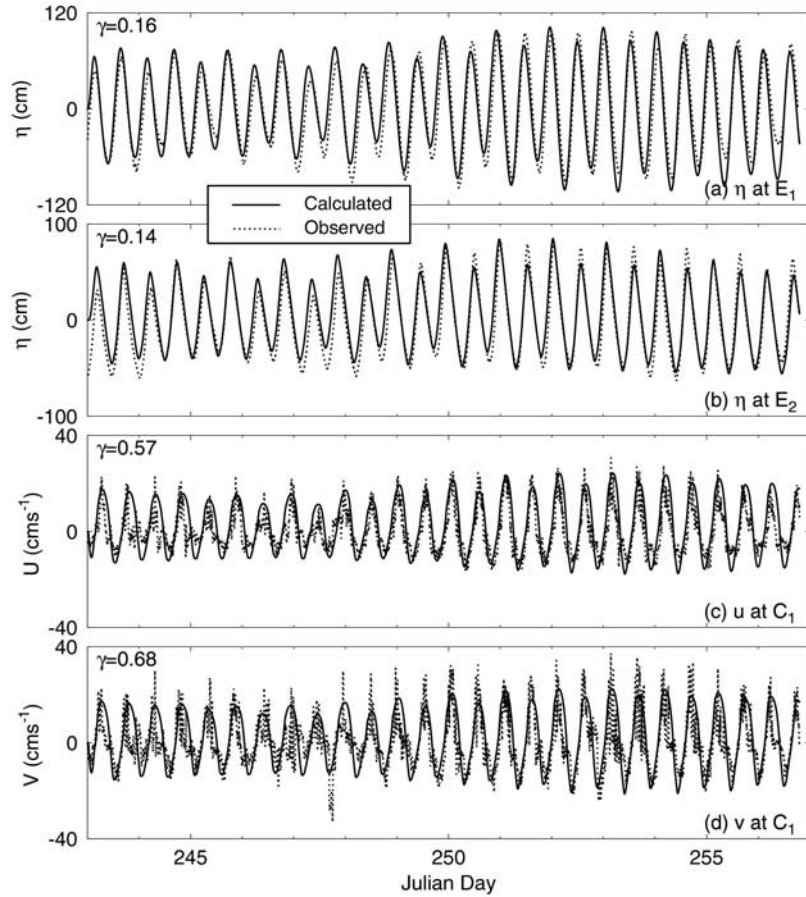


Figure 3. Time series of simulated and observed sea surface elevations at location (a) E_1 and (b) E_2 , and the (c) eastward and (d) northward components of the currents at location C_1 in September 1991. The subtidal variations of the observed currents with periods longer than 27 hours were filtered out, and the simulated currents are at 1 m above the seabed.

elevations at Lunenburg Harbour. We use this transfer function to update η_t and integrate the coastal circulation model again with the updated η_t . We repeat the above procedure if the model-calculated η_h^m does not agree with η_h^c . For the barotropic tidal circulations in LB, we found that one iteration of the above procedure is sufficient to determine η_t from η_h^c . It should be noted that the above ad hoc approach is equivalent to the so-called “incremental approach” to data assimilation [Courtier *et al.*, 1994; Lu *et al.*, 2001a], with CHS-predicted η_h^c treated as observations.

[18] The model-calculated surface elevations agree reasonably well with the observed bottom pressures at locations E_1 and E_2 (Figures 3a and 3b). To quantify the model performance, we follow Thompson and Sheng [1997] and use the γ^2 value defined as

$$\gamma^2 = \frac{\text{Var}(O - M)}{\text{Var}(O)} \quad (4)$$

to measure the model hindcast error, where Var represents the variance, O and M represent the observed and model-calculated variables respectively, such as surface elevations and currents in this study. Clearly, the smaller γ^2 , the better the hindcast skill of the model. Furthermore, we also have $\gamma^2 \geq \gamma_{\min}^2$. For the model results shown in Figures 3a and

3b, the γ^2 values are about 0.16 and 0.14 at locations E_1 and E_2 , respectively. The γ^2 value is about twice as large as the γ_{\min}^2 value at E_1 , but very close to the γ_{\min}^2 value at E_2 . Therefore the coastal circulation model performs reasonably well in hindcasting sea surface elevations, particularly at E_2 .

[19] We also compare the model-calculated currents with the observed currents at about 1 m from the seabed at C_1 (Figures 3c and 3d). The γ^2 value is 0.57 and 0.68 respectively for the eastward and northward components of the currents at this location, which are about twice as large as γ_{\min}^2 for both eastward and northward components.

[20] We next compare the simulated tidal circulation with the measurements made in the first 2 weeks of September 2003 (Figure 4), during which the wind forcing was also relatively weak. Similarly, the low-frequency variations of the observed currents were removed with a cutoff period of 27 hours. The tidal harmonic analysis indicates that tides with 17 constituents (including M_2 , S_2 , K_1 , O_1 , etc.) explain about 97% of the total variance of the observed bottom pressure at B_2 in LB and 90% with 9 tidal constituents at location M in USC. The M_2 tide at two locations account for about 85% (B_2) and 83% (M) of the total variance of the observed bottom pressure. Tides with 17 constituents account for about 53% and 51% of the total variance of the low-pass-filtered current measurements in the eastward and

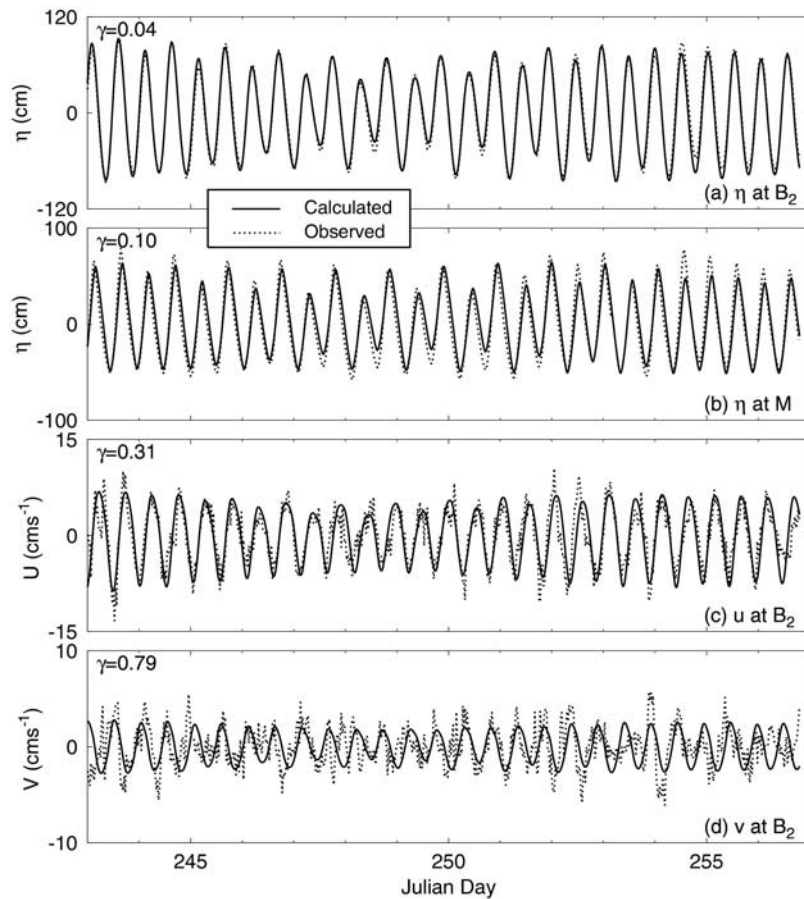


Figure 4. Time series of simulated and observed sea surface elevations at locations (a) B_2 and (b) M , and the (c) eastward and (d) northward components of the currents at location B_2 during the first 2 weeks of September 2003. The subtidal variations of the observed currents with periods longer than 27 hours were filtered out, and both observed and simulated currents are at depth of 7.5 m below the mean sea level.

northward directions at 7.5 m below the mean sea level at B_2 . The γ^2 values are 0.04 and 0.1 respectively for the surface elevation at B_2 and M , and 0.31 and 0.79 respectively for the eastward and northward components of currents at B_2 .

[21] In comparison with the model results in September of 1991, the coastal circulation model does less well in simulating the tidal currents in September 2003, for which there are two possible reasons. First, site B_2 is located at the entrance of LB, where bottom topography is less accurate than that over other areas of LB. This is because that the bottom topography for the study region was generated using Barnes' algorithm from several bathymetric data sets with different horizontal resolutions, which are about 40 m for the data sets in the interior and about 100 m for those over the outside of LB. To confirm this, we compare the observed and simulated tidal current ellipses at this site and found that the amplitude of the simulated M_2 ellipse (about 5.3 cm s^{-1}) is highly comparable to the observed one (about 5.0 cm s^{-1}), but there is a large difference in the orientation between the observed and simulated M_2 ellipses. (The simulated M_2 current ellipse is more east-westward than the observed one). Second, the observed water temperature at this site has significant temporal variabilities

at both the seasonal and M_2 frequency during this period (not shown), indicating the importance of the baroclinic circulation at this location.

4. Tidal Circulation and Nonlinear Dynamics of M_2

[22] As discussed above, the M_2 tide is the dominant constituent in the study region. In the rest of this paper, we force the fine-resolution coastal circulation model with the M_2 tide specified at the model open boundaries and examine the tidal circulation and associated nonlinear dynamics based on the model results. We use the same model parameters as in section 2 and integrate the fully nonlinear coastal circulation model for ten M_2 tidal cycles (referred to as the control run).

[23] The model-calculated surface elevations have negligible horizontal variations in LB and the two coves, respectively. There are, however, large differences in amplitude and phase between the simulated surface elevations over two areas (Figure 5a). The simulated amplitudes of surface elevations are about 0.63 m in LB and 0.45 m in USC, which agrees remarkably well with the observed amplitudes of 0.64 m in LB and 0.44 m in USC. The

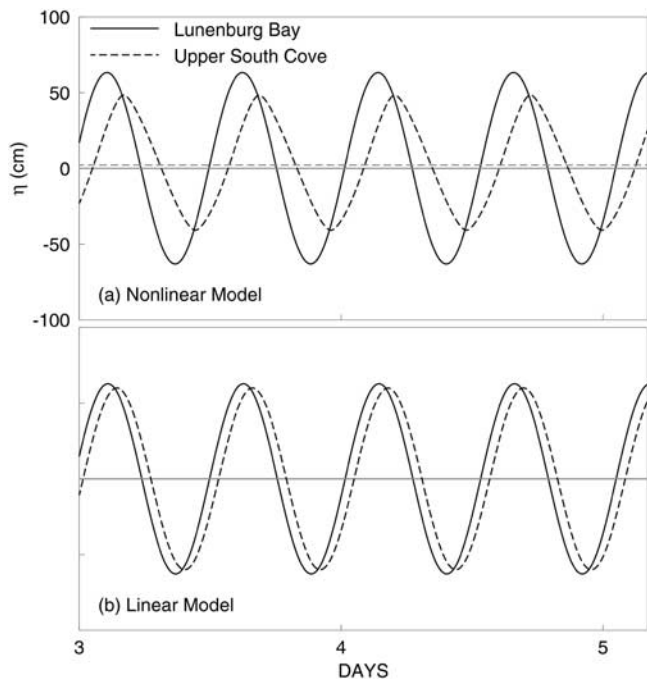


Figure 5. Time series of surface elevations in Lunenburg Bay and Upper South Cove produced by (a) a nonlinear model and (b) a linear model. Both models are forced by the M_2 tide at the model open boundaries. The shaded solid and dashed lines represent the tidally averaged (time mean) sea levels in Lunenburg Bay and Upper South Cove, respectively.

simulated surface elevation in LB peaks prior to that in USC by about one hour and forty two minutes, which also agrees reasonably well with the observed lag of about one hour and thirty minutes. The simulated surface elevation in LB is highly symmetric (Figure 5a). In comparison, the simulated surface elevation in USC has a large ebb-flood asymmetry, with a relatively sharp crest and shorter duration in water rising and a wide trough and longer duration in water falling. Furthermore, the coastal circulation model also produces a positive difference in the tidally averaged (time mean) sea levels between USC and LB, with the time mean sea level of about 2.3 cm in USC and zero in LB.

[24] To examine the role of the nonlinear tidal dynamics in generating the ebb-flood asymmetry in USC, we construct a linear tidal circulation model by eliminating the nonlinear terms in the momentum and continuity equations and using the linear bottom friction parameterization with the linear bottom friction coefficient set to 0.01 cm s^{-1} (see section 7 for more discussion of the linear bottom friction parameterization). Other model parameters are same as before. We force this linear model with the same semidiurnal tide as in the control run (Figure 5b). The surface elevations produced by the linear model are symmetric in both LB and USC, with a phase difference of about 50 min and an amplitude deduction of only about 5% between the USC and LB, which differ significantly from the model results in the control run (Figure 4). Furthermore, the linear model does not generate any positive difference in the tidally averaged sea level between USC and LB.

[25] To determine the role of the nonlinear bottom friction, we conduct an additional numerical experiment using the nonlinear bottom friction parameterization but excluding all the nonlinear terms in the momentum and continuity equations (see section 7 for more discussion). The model-calculated surface elevations in this experiment are very similar to those produced by the linear model. Therefore the nonlinear advection and nonlinear free surface (i.e., the nonlinear terms in the continuity equation) play a dominant role in generating the nonlinear characteristics of surface elevations in USC.

[26] We next calculate the current ellipses of M_2 from the model results in the control run during the tenth M_2 cycle. The near-surface M_2 current ellipses (Figure 6a) are relatively narrow and aligned roughly with the bottom topography over central and outer LB, and nearly rectilinear in the two coves. Over western LB, Corkum's Channel and their vicinity, however, the near-surface current ellipses vary significantly in shape and rotation. Typical amplitudes of the near-surface M_2 currents are about 25 cm s^{-1} over Corkum's Channel and adjacent areas, 10 cm s^{-1} in LB, and 5 cm s^{-1} over the two coves. The near-bottom current ellipses of M_2 are smaller than the near-surface ellipses (Figure 6b), except for USC, LSC, and the narrow mouth and channel connecting LB with the two coves. Over most part of these shallow areas the near-surface and near-bottom current ellipses are same since there is only one z level in the vertical. Typical amplitudes of the near-bottom M_2 tidal currents in LB are about 5 cm s^{-1} or less, which are smaller than the near-surface currents.

[27] To examine the energy flow associated with the M_2 tide in LB, we follow Greenberg [1979] and Davies and Kwong [2000] and compute the tidally averaged (time mean) energy flux vectors of M_2 based on

$$(E_x, E_y) = \frac{\rho_o}{T} \int_0^T \int_{-h}^{\eta} (u, v) \left[g\eta + \frac{u^2 + v^2}{2} \right] dz dt \quad (5)$$

where (E_x, E_y) are eastward and northward components of the M_2 energy flux vector, (u, v) are components of the horizontal velocity vector and η is surface elevation of M_2 , ρ_o and g denote respectively the water density and gravity acceleration, h is water depth, and T is the period of M_2 .

[28] The time mean tidal energy flux of M_2 enters LB through the western part of the transect between Ovens Point and East Point Island, with a maximum northwestward flux of about 1 kW m^{-1} (Figure 7). The time mean M_2 energy flux separates into two main branches over outer LB. These two branches merge over inner LB and form a jet-like energy flow that veers southwestward and then enters Corkum's Channel. There is a small amount of time mean M_2 energy flux that separates from the main branch before entering Corkum's Channel and flows southeastward along the west coast of LB. In the two coves, particularly in LSC, the time mean M_2 energy flux is very weak. Figure 7 also shows that there is a relatively large M_2 energy sink over the small area to the south end of Corkum's Channel due mainly to large tidal dissipations.

[29] To demonstrate the importance of the nonlinear tidal dynamics in the region, we calculate the first two harmonics (or overtides) of the semidiurnal tide: M_4 and M_6 , from the model results in the control run during the tenth M_2 cycle.

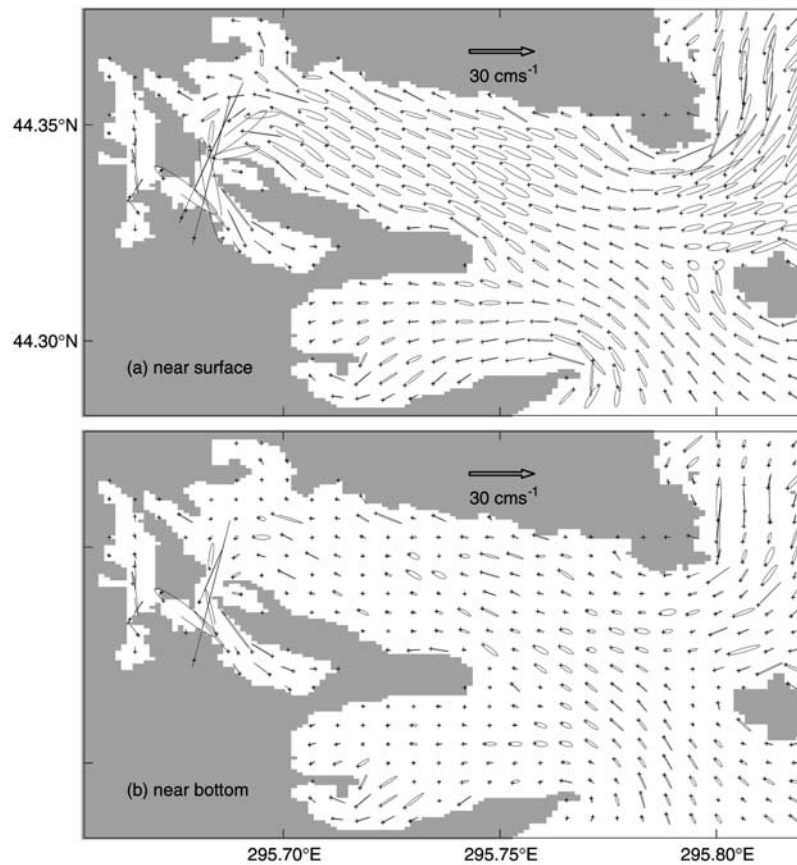


Figure 6. Current ellipses of M_2 calculated from the model results in the control run during the tenth M_2 tidal cycle at (a) the top z level and (b) the bottom z level. The model is forced by the M_2 tide at the model open boundaries. Current ellipses are plotted at every seventh model grid point. The plus represents the starting time, which is the same for each ellipse.

Figure 8 shows the near-surface current ellipses of overtidess M_4 and M_6 over western LB and two coves. The near-surface current ellipses of the overtide M_4 are relatively large over western LB, Corkum's Channel, northern LSC and southern USC, with a typical speed of about 3 cm s^{-1} .

The near-surface current ellipses of the overtide M_6 have similar horizontal distributions as the overtide M_4 , except for smaller amplitudes. The M_6 near-surface currents are relatively large over Corkum's Channel and adjacent areas, with a typical speed of about 1 cm s^{-1} . Our model results

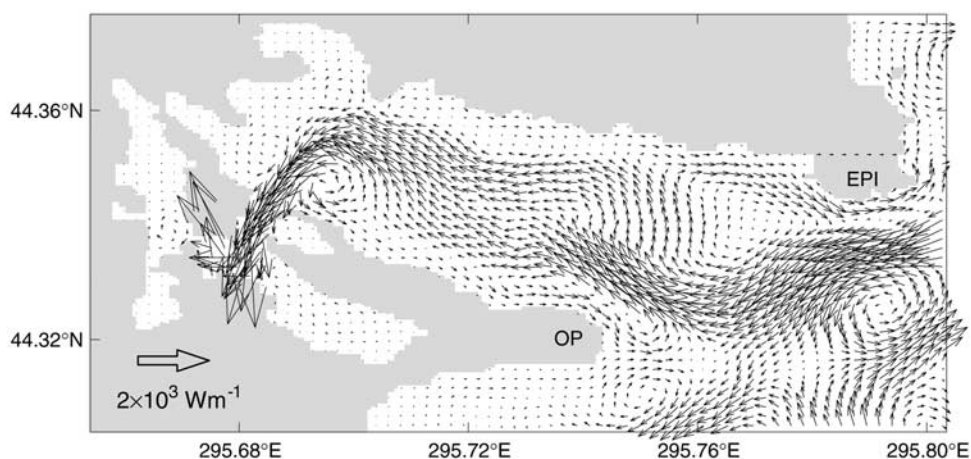


Figure 7. Time mean energy flux vectors of the M_2 tide calculated from the model results in the control run during the tenth M_2 tidal cycle. The energy flux vectors are plotted at every third model grid point. Abbreviations are used for East Point Island (EPI) and Ovens Point (OP).

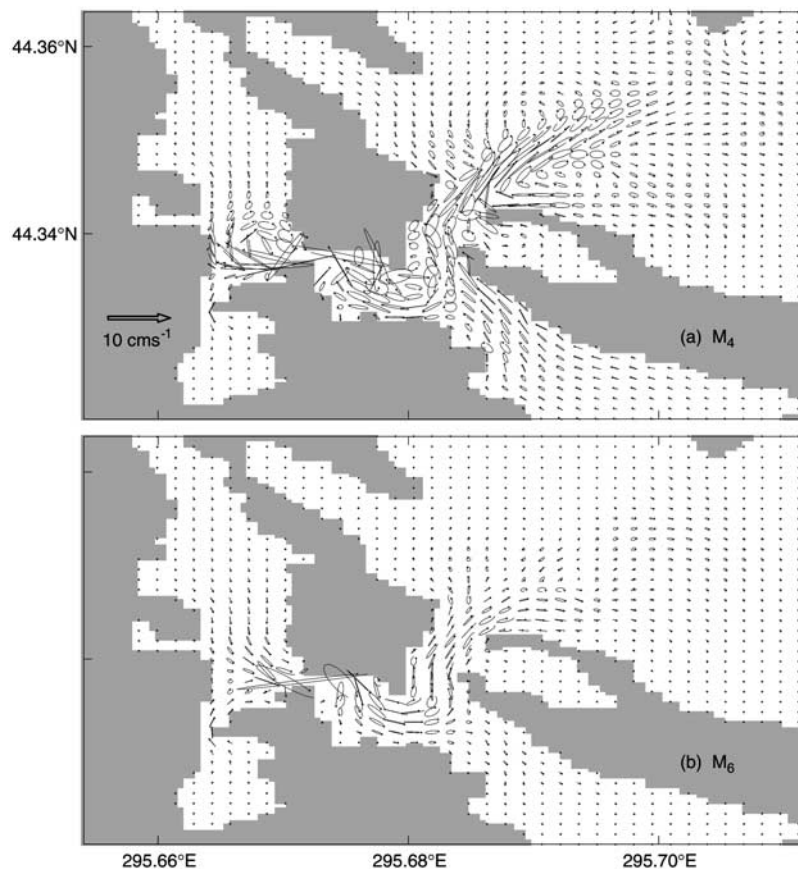


Figure 8. Near-surface current ellipses of overtidess (a) M_4 and (b) M_6 calculated from the model results in the control run during the tenth M_2 tidal cycle. The model is forced by the M_2 tide at the model open boundaries. Current ellipses are plotted at every second model grid point. The plus represents the starting time, which is the same for each ellipse.

also demonstrate that the overtide M_4 is predominately generated by the nonlinear advection terms in the momentum equation, while the overtide M_6 is predominantly generated by the quadratic bottom friction and nonlinear free surface, with some contribution from advection (see section 7 for more discussion), which are consistent with previous studies [Parker, 1991; Davies and Jones, 1996; Hench and Luettich, 2003]. Therefore the nonlinear advection, nonlinear free surface and quadratic bottom friction play a very important role in governing the tidal circulation over western LB, Corkum's Channel and adjacent areas.

5. Jet-Like Flow Along Corkum's Channel

[30] One of the important circulation features produced by the circulation model is a jet-like flow through Corkum's Channel (Figure 9). This jet-like flow was also simulated previously by Sturley *et al.* [1993] and Thompson *et al.* [1998] and confirmed by recent measurements made in the channel using a ship-mounted ADCP (A. Hay, personal communication, 2003). At maximum ebb (defined as the time of the maximum current during ebb tide over outer LB), the southeastward flow from USC and northwestward flow from LSC merge over the south end of Corkum's Channel and form an intense jet-like flow that runs northeastward along Corkum's Channel to western LB, with a

maximum speed of about 50 cm s^{-1} (Figure 9b). After exiting from Corkum's Channel, this jet-like flow spreads gradually over western LB. At maximum flood (defined as the time of the maximum current during flood tide over outer LB), the LB water converges over the north side of Corkum's Channel and forms a strong southwestward flow that enters the two coves through Corkum's Channel, with a maximum speed of about 40 cm s^{-1} (Figure 9d).

[31] In addition to the intense tidal jet through Corkum's Channel, the circulation model also generates a large along-channel surface elevation drop of about 4.0 cm at maximum ebb (Figure 9a) and a moderate along-channel jump of about 3.0 cm at maximum flood over about 1 km distance from the south end to the north end of Corkum's Channel (Figure 9c). In comparison, the model-calculated surface elevations have much smaller spatial variations outside Corkum's Channel, including the areas where the tidal currents are relatively strong. Therefore many physical processes other than the horizontal pressure gradient are also at work over Corkum's Channel and adjacent areas.

[32] Figure 10 shows the vertical distributions of horizontal (i.e., along-transect) and vertical components of the jet-like flow along a transect marked in Figure 9c. This transect is roughly along the central axis of the jet-like flow as it runs from the south end of Corkum's Channel to western LB during ebb tide. The offshore distance in Figure 10 is

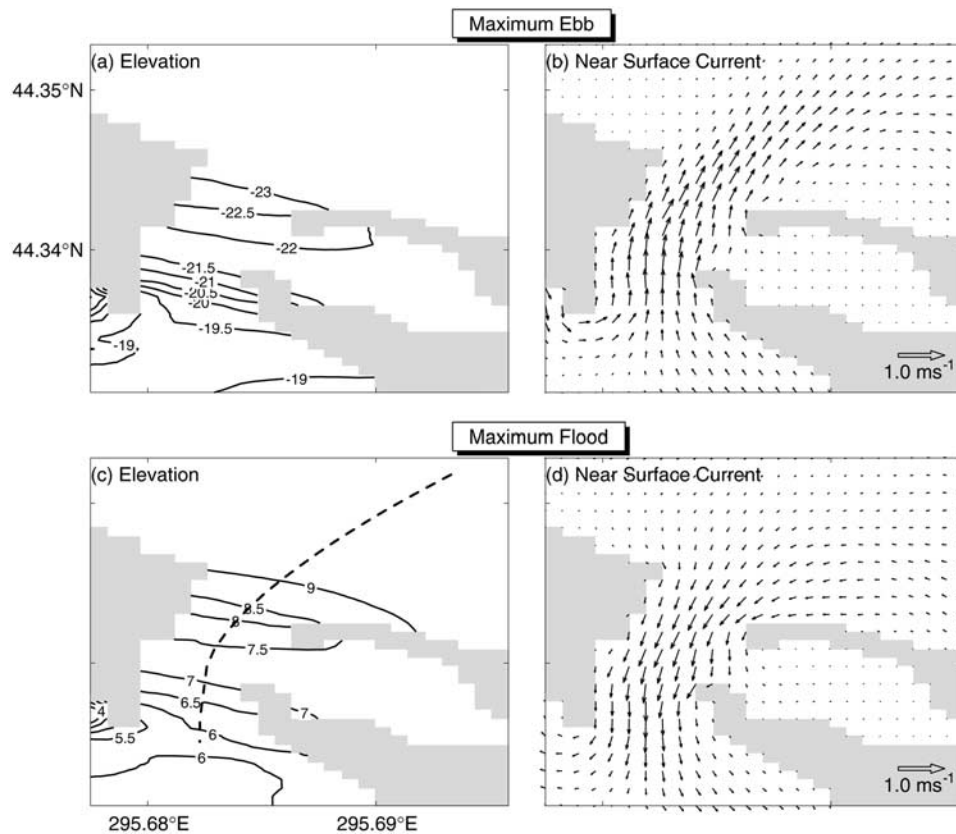


Figure 9. Model-calculated surface elevations and near-surface currents over Corkum's Channel and adjacent western Lunenburg Bay at (a) and (b) maximum ebb and (c) and (d) maximum flood. Contours in Figures 9a and 9c are labeled in centimeters. The dashed line in Figure 9c represents a transect, along which the model results are presented in Figures 10 and 11. The transect is roughly along the central axis of the tidal jet during ebb.

measured from the south end of Corkum's Channel along the transect, with the north end of Corkum's Channel located at the offshore distance of about 1 km (Figure 9c). The horizontal and vertical components shown in Figure 10 are interpolated from the model-calculated currents. During ebb tide (Figures 10a and 10b), a strong jet-like flow runs northeastward with a typical speed of about 40 cm s^{-1} along the southwestern portion of the transect (referred to as the inner transect) with the offshore distances of less than 1 km. After emanating from Corkum's Channel, the jet-like flow continues to run northeastward and then spreads horizontally and vertically along the northeastern portion of the transect (referred to as the outer transect) with the offshore distances greater than 1 km. The magnitudes of outward currents during ebb decrease significantly with offshore distance and depth (Figures 10a and 10b). During flood tide, the western LB water flows southwestward and forms a southwestward jet-like flow over Corkum's Channel. Figure 10 also shows that the vertical component of the jet-like flow along the outer transect is relatively large and mainly downward during ebb tide and relatively weak, but still well organized during flood tide. In comparison with the horizontal component of the flow, however, the vertical component is about 2 orders of magnitude smaller (Figure 10).

[33] We follow *Hench et al.* [2002] and *Hench and Luettich* [2003] and examine the transient momentum balance of the jet-like flow. Figure 11 shows the instanta-

neous magnitudes of four terms (i.e., local acceleration, horizontal pressure gradient, nonlinear advection and horizontal/vertical mixing) in the horizontal momentum equation along the same transect as in Figure 10. The Coriolis term is not presented since its magnitude is very small in comparison with other momentum equation terms. The transient momentum balance at maximum ebb (Figures 11a–11d) is primarily between the horizontal pressure gradient, nonlinear advection and tidal mixing along the inner transect, where the local acceleration is relatively small except for the lower water column near the bottom (Figure 11a). Along the outer transect, tidal mixing at maximum ebb is small and the transient balance is mainly between the local acceleration, nonlinear advection and horizontal pressure gradient. At maximum flood, all the four momentum equation terms (i.e., local acceleration, horizontal pressure gradient, advection and tidal mixing) are important along the inner transect (Figures 11e–11h). Along the outer transect, the transient momentum balance is primarily among the horizontal pressure gradient, nonlinear advection and tidal mixing at maximum flood.

6. Residual Circulation and Tidally Averaged Momentum Balance

[34] The nonlinear interaction of the tidal oscillatory flow with local topography also generates residual circulation in

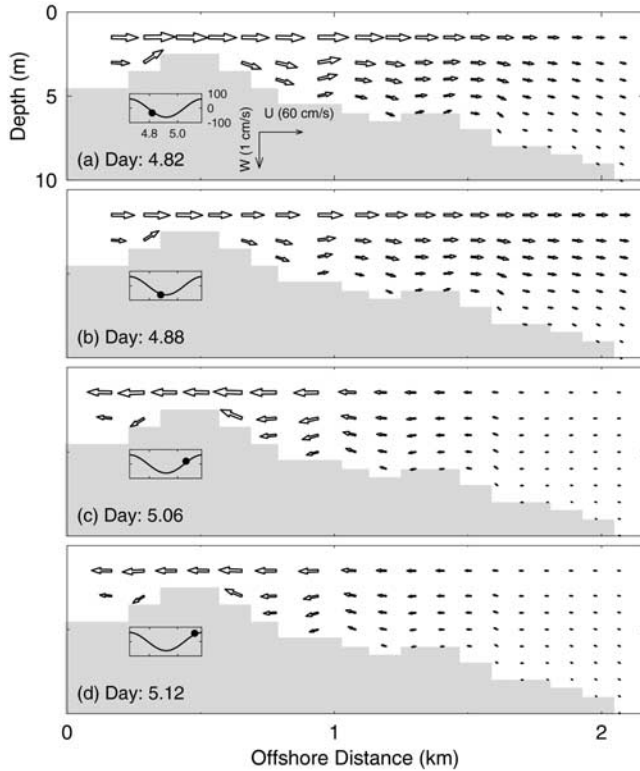


Figure 10. Distributions of horizontal (along transect) and vertical components of the tidal jet along the transect marked in Figure 9c at (a) and (b) ebb tide and (c) and (d) flood tide.

the coastal embayments and tidal inlets. *Nihoul and Ronday* [1975] introduced the “tidal stress” concept in the study of the time mean circulation in the Southern Bight of the North Sea. Their tidal stress represents the tidally averaged nonlinear terms in the continuity and momentum equations. *Tee* [1976, 1981] examined the two- and three-dimensional structures of the tide-induced residual currents. *Zimmerman* [1978] demonstrated that the production of residual circulation depends on the amplitude of tidal displacement relative to the integral length scale of the bottom irregularities. *Robinson* [1981] examined the nonlinear dynamics of the circulatory residuals based on the depth-averaged vorticity equation. *Imasato* [1983] demonstrated that the tide-induced residual circulation near a narrow strait is the result of the averaging process of the tide-induced transient eddy. *Ridderinkhof and Zimmerman* [1990] examined the tidally averaged vorticity balance in the western Dutch Wadden Sea. There is however a lack of previous research work on the physical processes responsible for the residual flows associated with an intense jet-like flow.

[35] To examine the role of various nonlinear terms in generating the residual flows associated with the jet through Corkum’s Channel, we calculate the depth-mean tidally averaged residual flow from the model results forced by the M_2 forcing in the control run during the tenth M_2 tidal cycle (Figure 12). The depth-mean residual flow is characterized as a relatively large-scale anticyclonic recirculation over western LB and several small-scale recirculations in the two coves close to the narrow mouth. The residual flow

is rather weak over outer LB, northern USC and southern LSC. In comparison with jet flow in LB the depth-mean residual flow demonstrates very similar distributions. In fact, residual flow in this region reflects the time-mean jet flow during a period of M_2 tide. Both flows are dynamically associated with each other.

[36] To identify the dominant physical processes responsible for the residual flow shown in Figure 12, we decompose the horizontal components of the model currents ($\vec{u} = u\hat{i} + v\hat{j}$) into two parts: the periodic tidal flow ($\vec{u}' = u'\hat{i} + v'\hat{j}$) and time-mean flow ($\vec{u} = U\hat{i} + V\hat{j}$), where \hat{i} and \hat{j} are the unit vectors in the eastward and northward components, respectively. We integrate the horizontal momentum equations (A1) and (A2) in Appendix A over one tidal cycle and yield the following tidally averaged momentum equation:

$$\nabla \cdot (\overline{\vec{u}'\vec{u}'}) = -g\nabla_h \bar{\eta} - \nabla \cdot (\vec{U}\vec{U}) + \nabla_h \cdot (A_m \nabla_h \vec{U}) + \frac{\partial}{\partial z} \left(K_m \frac{\partial \vec{U}}{\partial z} \right) - F\hat{k} \times \vec{U} \quad (6)$$

where the overbar represents the time mean over a tidal cycle, $\nabla_h = \hat{i}\frac{\partial}{\partial x} + \hat{j}\frac{\partial}{\partial y}$, $\nabla = \nabla_h + \hat{k}\frac{\partial}{\partial z}$, and \hat{k} is the unit vector in the upward direction. The term on the left-hand side of equation (6) (i.e., $\nabla \cdot (\overline{\vec{u}'\vec{u}'})$) is the tidally averaged advection of the oscillatory currents resulting from the nonlinear interaction of tidal currents with the local bathymetry. This term is part of “tidal stress” suggested by *Nihoul and Ronday* [1975] and is the forcing term for the residual flow. This forcing term is balanced by five terms on the right-hand side of equation (6). They are the time mean horizontal pressure gradient: $-g\nabla_h \bar{\eta}$; advection of the residual flow: $\nabla \cdot (\vec{U}\vec{U})$; time mean dissipation due to lateral and bottom boundaries: $\nabla_h \cdot (A_m \nabla_h \vec{U}) + \frac{\partial}{\partial z} (K_m \frac{\partial \vec{U}}{\partial z})$ and time mean Coriolis term: $F\hat{k} \times \vec{U}$.

[37] We calculate all six terms in (6) from the model results in the control run during the tenth M_2 cycle. For simplicity, we only compare the magnitudes of these terms in the top z level in this study. The tidally averaged advection of the oscillatory currents ($|\nabla \cdot (\overline{\vec{u}'\vec{u}'})|$) in the top z level is relatively large over the areas with large residual flow (Figure 13a), particularly over the narrow channel and mouth connecting LB and two coves and adjacent areas, with a maximum magnitude of about 0.12 cm s^{-2} after smoothing (Table 1). The tidally averaged horizontal pressure gradient ($|g\nabla_h \bar{\eta}|$) has similar spatial distributions to the forcing term, with large values over Corkum’s Channel and environs (Figure 12b). The maximum value of ($|g\nabla_h \bar{\eta}|$) in the study region is about 0.11 cm s^{-2} , which is about 93% of the maximum value of $|\nabla \cdot (\overline{\vec{u}'\vec{u}'})|$. It should be noted that the maximum magnitudes of the six dynamic terms in (6) do not occur, in general, at the same location.

[38] The tidally averaged advection of the residual flow ($|\nabla \cdot (\vec{U}\vec{U})|$) are large mainly over the narrow mouth between the two coves and relatively small over other areas, with the maximum magnitude of about 0.03 cm s^{-2} , which is about 23% of the maximum value of the forcing term. The tidally averaged tidal dissipation ($|\nabla_h \cdot (A_m \nabla_h \vec{U}) + \frac{\partial}{\partial z} (K_m \frac{\partial \vec{U}}{\partial z})|$) in the top z level has different spatial patterns from the forcing term, with a maximum magnitude of about 0.09 cm s^{-2} , which is about 78% of the maximum magni-

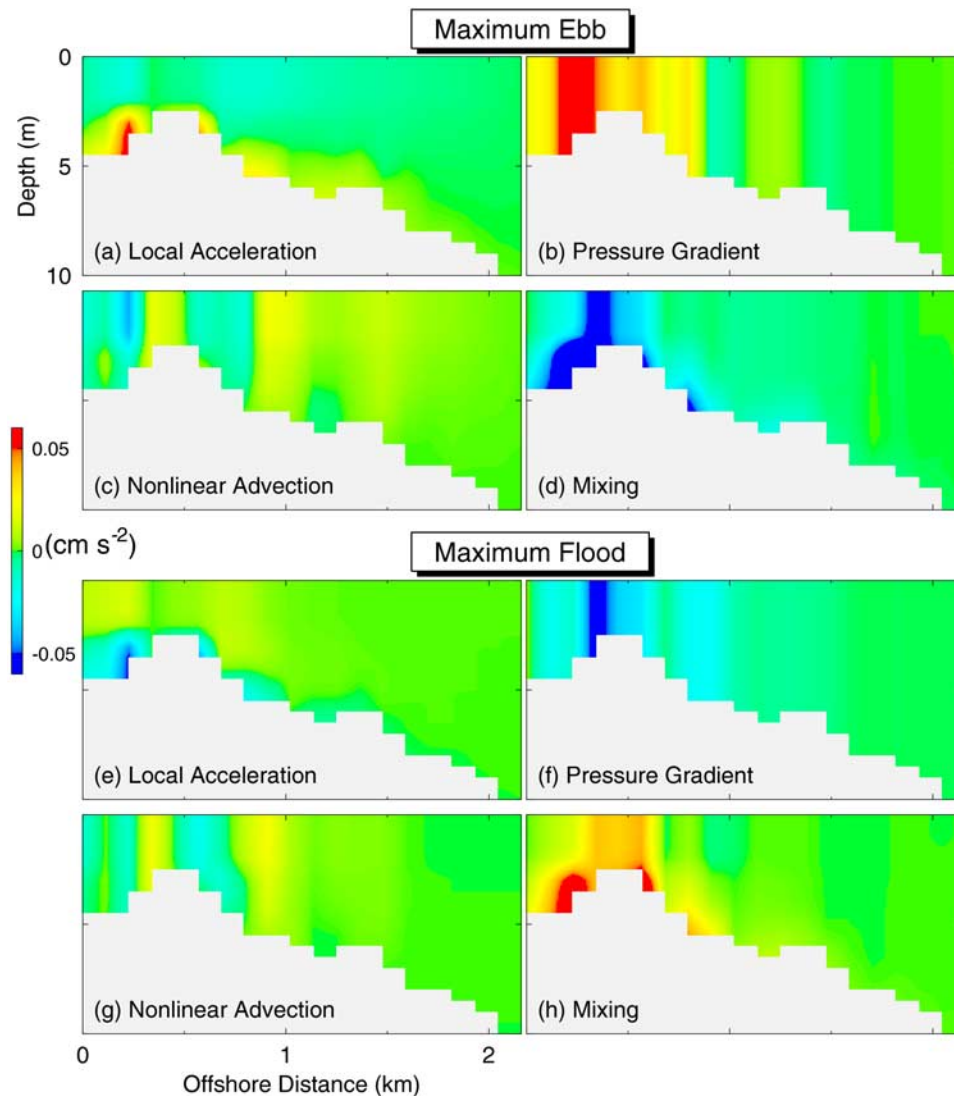


Figure 11. Vertical distributions of four momentum equation terms: (a) and (e) local acceleration, (b) and (f) horizontal pressure gradient, (c) and (g) nonlinear advection, and (d) and (h) tidal mixing along the transect marked in Figure 8c. A three-point moving average filter is used to eliminate small-scale features that are not well presented in the figure. Positive values mean roughly northeastward along the transect.

tude of the forcing term. The tidally averaged Coriolis term is small everywhere, with a maximum magnitude is about 2% of that of the forcing term. Therefore the main dynamic balance for the residual flow of M_2 in the study region is the nonlinear interaction of tidal oscillatory currents with local bathymetry, tidally averaged horizontal pressure gradient, and lateral and bottom tidal dissipation. The advection of the residual flow also plays an important role in generating the residual flow over western LB, Corkum's Channel and adjacent areas. The Earth's rotation, on the other hand, plays a very minor role in driving the residual flow of M_2 in the study region.

7. Sensitivity Studies

[39] We conduct three additional numerical experiments to examine the sensitivity of the model-produced nonlinear characteristics of tidal circulation in western LB, Corkum's Channel and their vicinities to three types of the nonlinear

physics retained in the model (i.e., nonlinear terms in the continuity equation, nonlinear terms in the horizontal momentum equation, and the quadratic bottom friction parameterization). The coastal circulation model in these three experiments is forced by the same M_2 tide at the model open boundaries with the same model parameters as in the control run, except where otherwise noted.

[40] In the first experiment we run the linear free surface version of CANDIE that includes the advection terms in the momentum equation and quadratic bottom friction but excludes the nonlinear terms in the continuity equation (referred to as the linear continuity equation case). The near-surface current ellipses of the overtides M_4 and M_6 in this case (Figures 14a and 14b) are in reasonable agreement with those in the control run (Figure 8), except for some differences in small-scale features over the vicinity of the narrow month connecting the two coves. Therefore the nonlinear terms in the continuity equation do not play a dominant role in generating overtides M_4 and M_6 in the

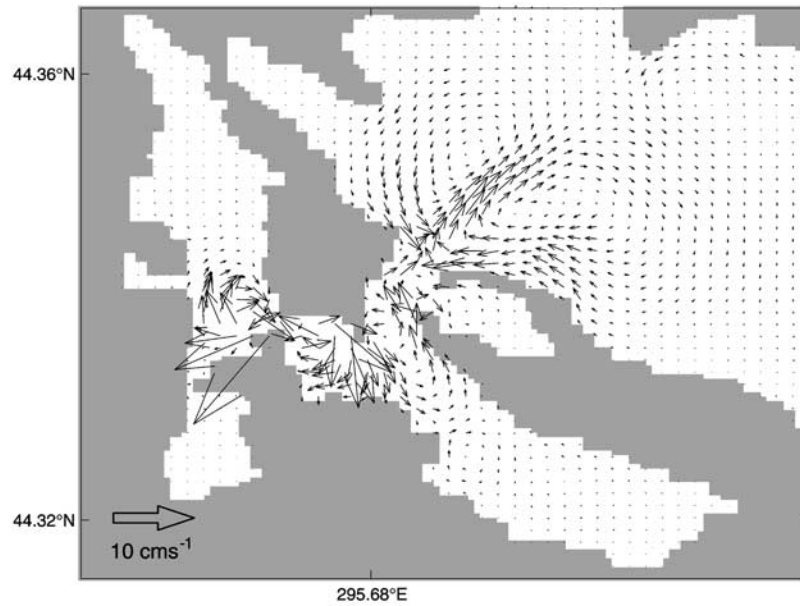


Figure 12. Depth mean residual flow in western Lunenburg Bay and the two coves calculated from the three-dimensional model results forced by the M_2 forcing at the model open boundaries during the tenth M_2 tidal cycle. Current vectors are plotted at every second model grid point.

study region. It should be noted, however, that the nonlinear free surface plays an important role in generating the ebb-flood asymmetry of the surface elevations in USC as discussed in section 4.

[41] We also run the linear free surface version of CANDIE in the second experiment using the quadratic

bottom friction but excluding the advection terms and nonlinear terms in the continuity equation (referred to as the linear continuity and momentum equations case). The near-surface currents of the overtide M_4 in this case is negligible (Figure 14c). The near-surface current ellipses of the overtide M_6 (Figure 14d) have similar horizontal

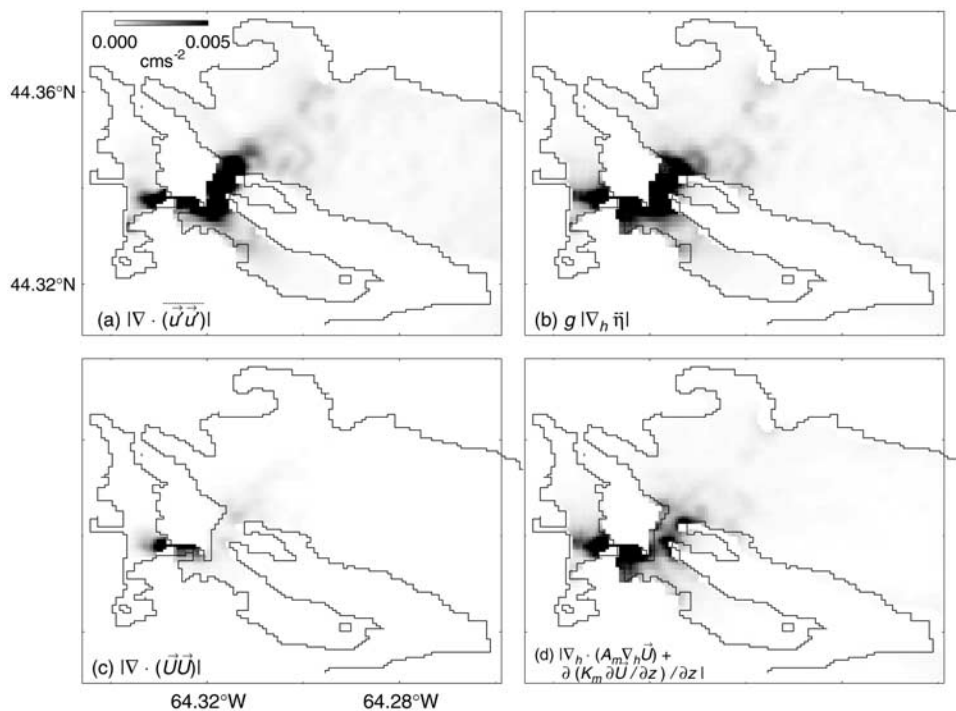


Figure 13. Magnitudes of the four dynamic terms in the tidally averaged momentum equation in the top z level. A three-point moving average filter is used to eliminate small-scale features that are not well presented in the figure. (a) Tidally averaged advection of the oscillatory flow (i.e., the nonlinear interaction of tidal oscillatory currents with local bathymetry), (b) tidally averaged horizontal pressure gradients, (c) tidally averaged advection of the residual flow, (d) tidally averaged lateral and bottom tidal dissipation.

Table 1. Maximum Magnitudes (in Units of cm s^{-2}) of Dynamic Terms in the Tidally Averaged Momentum Equation (6) and Percentages of Each Term Relative to the Forcing Term (i.e., Tidally Averaged Advection of the Oscillatory Flow: $|\nabla \cdot (\bar{u}'\bar{u}')|$) in Lunenburg Bay and the Two Coves

	$ \nabla \cdot (\bar{u}'\bar{u}') $	$ g\nabla_h \bar{\eta} $	$ \nabla \cdot (\bar{U}\bar{U}) $	$ \nabla_h \cdot (A_m \nabla_h \bar{U}) + \frac{\partial}{\partial z} (K_m \frac{\partial \bar{U}}{\partial z}) $	$ \hat{f}k \times \bar{U} $
Maximum magnitude	0.120	0.112	0.028	0.093	0.002
Percentage, %	100	93	23	78	2

distributions as those in the control run, except for smaller amplitudes. The model results in the first two cases demonstrate that the overtide M_4 is generated primarily by the advection terms in the momentum equation [Parker, 1991], with some contribution from the nonlinear free-surface over the vicinity of the narrow month connecting the two coves. The quadratic bottom friction does not affect the overtide M_4 . The overtide M_6 is mainly produced by the quadratic bottom friction and the nonlinear terms in the momentum equation.

[42] In the third experiment, we run the nonlinear free-surface version of CANDIE with the linear bottom friction parameterization (referred to as the linear bottom friction case). The model in this case includes all the nonlinear

terms in the continuity and momentum equations. The linear bottom friction parameterization is expressed as:

$$\vec{\tau}_b = \rho_o r_b \vec{u}_b \quad (7)$$

where r_b is the linear bottom friction coefficient to be estimated from the tidally averaged value of $C_d |\vec{u}_b|$. For a near-bottom M_2 tidal current of 5 cm s^{-1} in amplitude, which is a typical value in the vicinity of Corkum's Channel (Figure 6b), we have $r_b \approx 3.0 \times 10^{-3} \times 2/\pi \times 5 \text{ cm s}^{-1} \approx 0.01 \text{ cm s}^{-1}$. Figures 14e and 14f shows the near-surface current ellipses of the overtides M_4 and M_6 in the linear bottom friction case with $r_b = 0.01 \text{ cm s}^{-1}$. The near-surface currents of M_4 and M_6 in this case have similar amplitudes

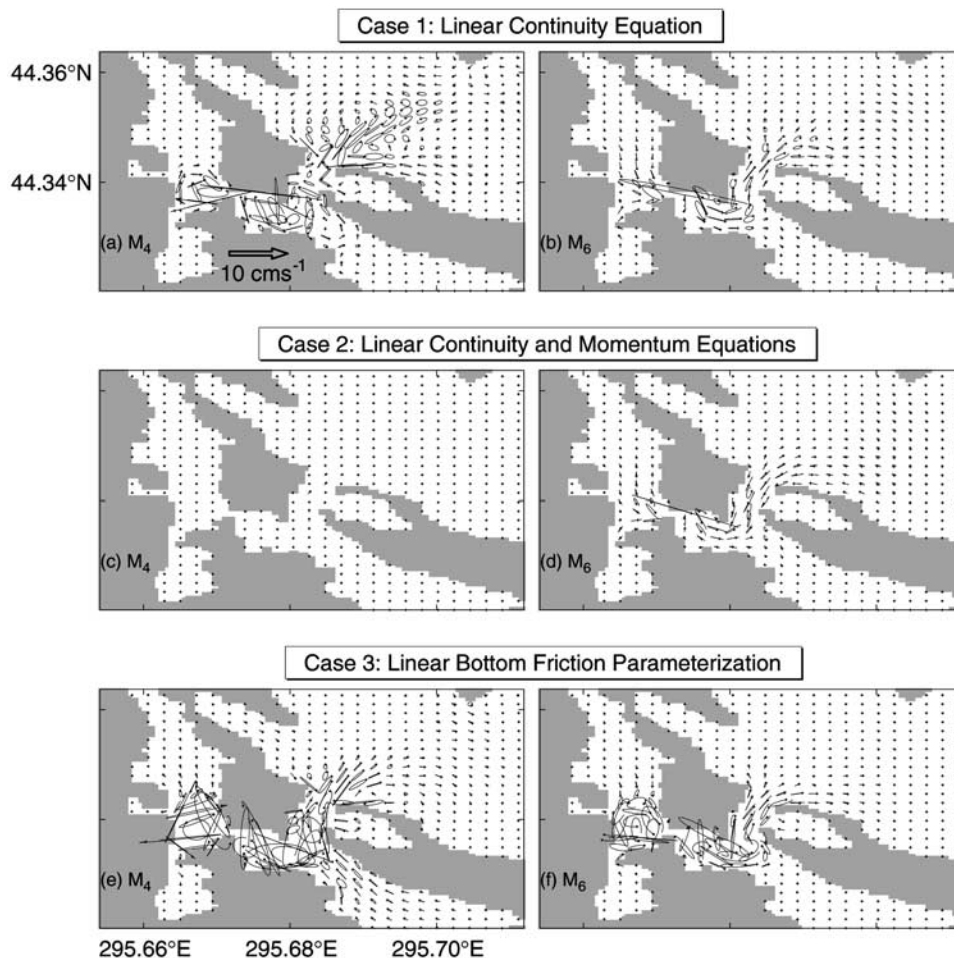


Figure 14. Near-surface current ellipses of overtides M_4 and M_6 calculated from the model results during the tenth M_2 tidal cycle in (a) and (b) the linear continuity equation case, (c) and (d) the linear continuity and momentum equations case, and (e) and (f) linear bottom friction case. Other model parameters are the same as in the control run. Current ellipses are plotted at every second model grid point. The plus represents the starting time, which is the same for each ellipse.

over Corkum's Channel and environs but are relatively smaller over western LB, in comparison with the control run (Figure 8). The overtides M_4 and M_6 in this case are, however, very sensitive to the value of r_b . The overtides M_4 and M_6 are smaller for the larger r_b . This further demonstrates the importance of the quadratic bottom friction parameterization in generating the nonlinear characteristics of the tidal circulation in the study region.

8. Summary and Discussion

[43] A three-dimensional, high-resolution coastal circulation model was used to study the barotropic tidal circulation and nonlinear dynamics in Lunenburg Bay (LB). The coastal circulation model is based on the three-dimensional, primitive equation ocean circulation model known as CANDIE with a nonlinear free surface and the fourth-order numerics. CANDIE has been applied to various modeling problems in the shelf. This study was the first time that CANDIE was used to simulate the high-resolution tidal circulation over the coastal water. In this study we ran the coastal circulation model in barotropic mode by setting model temperature and salinity to be invariant in time and space. We used the observed bottom pressures and currents made in LB in Septembers of 1991 and 2003 to assess the model performance. We forced the model with the tidal forcing specified at the model open boundaries using a simplified version of the incremental approach to data assimilation. The model results reproduce reasonably well the observed surface elevations, but less well the observed currents in the study region, which deserves a further study. The model results also reproduce reasonably well the intense jet through Corkum's Channel, which is one of the important circulation features in the study region.

[44] Although many aspects of nonlinear tidal dynamics are well known, there was less previous research work on the examination and quantification of nonlinear processes in generating an intense jet and associated residuals. In this study, we calculated the first two overtides of the semidiurnal tide: M_4 and M_6 , from the model results forced by the semidiurnal tide specified at the model open boundaries. The overtide M_4 is relatively large over western LB, Corkum's Channel and adjacent areas. The overtide M_6 is also relatively large over these areas, but with much smaller amplitude. We demonstrated that the overtide M_4 is produced primarily by the advection terms with some contribution from the nonlinear terms in the continuity equation, while the overtide M_6 is produced mainly by the quadratic bottom friction and nonlinear terms in the momentum equation, which are consistent with previous studies [Parker, 1991; Hench and Luettich, 2003]. We also demonstrated that the nonlinear terms in the continuity equation plays a dominant role in generating the ebb-flood asymmetry of the surface elevation in Upper South Cove.

[45] We followed Hench *et al.* [2002] and Hench and Luettich [2003] and examined the transient momentum balance of the tidal jet along a transect that is along roughly the central axis of the jet during ebb. We demonstrated that the local acceleration, horizontal pressure gradient, nonlinear advection and horizontal/vertical mixing play a very important role in the transient momentum balance within Corkum's Channel at maximum ebb and flood. Over

western LB, the transient balance is mainly between the local acceleration, nonlinear advection and horizontal pressure gradient at maximum ebb and between the horizontal pressure gradient and tidal mixing at maximum tide. The Coriolis term plays a minor role in comparison with other momentum equation terms in the study region.

[46] We also used the tidally averaged horizontal momentum equation to identify the main physical processes responsible for the residual flow of the M_2 tide in the study region. The main dynamic terms for the residual flow in the region are the tidally averaged advection of the oscillatory currents with bathymetry, tidally averaged pressure gradient and tidally averaged tidal dissipation. The time mean advection of the residual flow also plays an important role. The time mean Coriolis effect, on the other hand, plays a secondary role for the tidal circulation and residual flow in the region.

Appendix A: Basic Equations of the Ocean Circulation Model

[47] The three-dimensional primitive equation ocean circulation model known as CANDIE (<http://www.phys.ocean.dal.ca/programs/CANDIE>) [see Sheng *et al.*, 1998, 2001; Lu *et al.*, 2001b] with a free surface is used in this study. The governing equations of the model can be written in spherical coordinates as

$$\frac{\partial u}{\partial t} + \mathcal{L}u - \left(f + \frac{u \tan \phi}{R} \right) v = -\frac{1}{R \cos \phi} \frac{\partial(\eta + p_b/\rho_o)}{\partial \lambda} + \mathcal{D}_m u + \frac{\partial}{\partial z} \left(K_m \frac{\partial u}{\partial z} \right), \quad (\text{A1})$$

$$\frac{\partial v}{\partial t} + \mathcal{L}v + \left(f + \frac{u \tan \phi}{R} \right) u = -\frac{1}{R} \frac{\partial(\eta + p_b/\rho_o)}{\partial \phi} + \mathcal{D}_m v + \frac{\partial}{\partial z} \left(K_m \frac{\partial v}{\partial z} \right), \quad (\text{A2})$$

$$\frac{\partial \eta}{\partial t} = -\frac{1}{R \cos \phi} \left(\frac{\partial \int_{-h}^{\eta} u dz}{\partial \lambda} + \frac{\partial (\int_{-h}^{\eta} v \cos \phi dz)}{\partial \phi} \right), \quad (\text{A3})$$

$$\frac{\partial w}{\partial z} = -\frac{1}{R \cos \phi} \left(\frac{\partial u}{\partial \lambda} + \frac{\partial (v \cos \phi)}{\partial \phi} \right), \quad (\text{A4})$$

$$p_b = g \int_z^0 \rho dz', \quad (\text{A5})$$

$$\rho = \rho(T, S, p) \quad (\text{A6})$$

where u , v , w are the east (λ), north (ϕ) and vertical (z) components of the velocity vector \vec{u} , η is the surface elevation, $z = -h(x, y)$ is the position of the sea bottom, p is pressure, ρ is density, T and S are the potential temperature and salinity, p_b is the density-driven internal pressure, K_m

and K_h are vertical eddy viscosity and diffusivity coefficients, f is the Coriolis parameter, ρ_o is a reference density, R and g are the Earth's radius and gravitational acceleration, \mathcal{L} is an advection operator defined as

$$\mathcal{L}q = \frac{1}{R \cos \phi} \frac{\partial(uq)}{\partial \lambda} + \frac{1}{R \cos \phi} \frac{\partial(vq \cos \phi)}{\partial \phi} + \frac{\partial(wq)}{\partial z} \quad (\text{A7})$$

and \mathcal{D}_m and \mathcal{D}_h are diffusion operators defined as

$$\mathcal{D}_{(m,h)}q = \frac{1}{R^2} \left[\frac{1}{\cos^2 \phi} \frac{\partial}{\partial \lambda} \left(A_{(m,h)} \frac{\partial q}{\partial \lambda} \right) + \frac{\partial}{\partial \phi} \left(\cos \phi A_{(m,h)} \frac{\partial q}{\partial \phi} \right) \right] \quad (\text{A8})$$

where A_m and A_h are horizontal eddy viscosity and diffusivity coefficients, respectively. The model also uses the fourth-order numerics [Dietrich, 1997] and Thurnburn's flux limiter to discretize the nonlinear advection terms [Thurnburn, 1996].

[48] **Acknowledgments.** We wish to thank Richard Greatbatch, Youyu Lu, Alan Davis, Michael Dowd, Tony Bowen, Keith Thompson, Alex Hay, Doug Schillinger and two anonymous reviewers for their useful suggestions and comments. We also thank Charles O'Really for providing the sea level tidal prediction at Lunenburg Harbour. This project is part of the Centre for Marine Environmental Prediction (CMEP) supported by the Canada Foundation for Innovation (CFI) and Canadian Foundation for Climate and Atmosphere Study (CFCAS). J.S. is also supported by the Natural Sciences and Engineering Research Council of Canada (NSERC), MARTEC (a Halifax based company), and the Meteorological Service of Canada (MSC) through the NSERC/MARTEC/MSC Industrial Research Chair in "Regional Ocean Modeling and Prediction."

References

- Bowden, K. F. (1978), Physical problems of the benthic boundary layer, *Geophys. Surv.*, **3**, 255–296.
- Chadwick, D. B., and J. L. Largier (1999), Tidal exchange at the bay-ocean boundary, *J. Geophys. Res.*, **104**, 29,901–29,924.
- Courtier, P., J. N. Thepaut, and A. Hollingsworth (1994), A strategy for operation implementation of 4D-var, using an incremental approach, *Q. J. R. Meteorol. Soc.*, **120**, 1367–1387.
- Davidson, F., R. J. Greatbatch, and B. deYoung (2001), Asymmetry in the response of a stratified coastal embayment to wind forcing, *J. Geophys. Res.*, **106**, 7001–7016.
- Davies, A. M. (1993), A bottom boundary layer-resolving three-dimensional tidal model: A sensitivity study of eddy viscosity formulation, *J. Phys. Oceanogr.*, **23**, 1437–1453.
- Davies, A. M., and R. A. Flather (1978), Computing extreme meteorologically induced currents, with application to the northwest European continental shelf, *Cont. Shelf Res.*, **7**, 643–683.
- Davies, A. M., and J. E. Jones (1996), Sensitivity of tidal bed stress distributions, near bed currents, overtides and tidal residuals to frictional effects in the eastern Irish Sea, *J. Phys. Oceanogr.*, **26**, 2553–2575.
- Davies, A. M., and S. C. M. Kwong (2000), Tidal energy fluxes and dissipation on the European continental shelf, *J. Geophys. Res.*, **105**, 21,969–21,989.
- Dietrich, D. E. (1997), Application of a modified Arakawa 'a' grid ocean model having reduced numerical dispersion to the Gulf of Mexico circulation, *Dyn. Atmos. Oceans*, **27**, 201–217.
- Dowd, M. (1997), On predicting the growth of cultured bivalves, *Ecol. Modell.*, **104**, 113–131.
- Dukowicz, J. K., and R. D. Smith (1994), Implicit free-surface method for the Bryan-Cox-Semtner ocean model, *J. Geophys. Res.*, **99**, 7991–8014.
- Grant, J., M. Dowd, K. Thompson, C. Emerson, and A. Hatcher (1993), Perspectives on field studies and related biological models of bivalve growth and carrying capacity, in *Bivalve Filter Feeders and Marine Ecosystem Processes*, edited by R. Dame, pp. 371–420, Springer-Verlag, New York.
- Greenberg, D. A. (1979), A numerical model investigation of tidal phenomena in the Bay of Fundy and Gulf of Maine, *Mar. Geod.*, **2**, 161–187.
- Hench, L. H., and R. A. Luettich (2003), Transient tidal circulation and momentum balances at a shallow inlet, *J. Phys. Oceanogr.*, **33**, 913–932.
- Hench, L. H., B. O. Blanton, and R. A. Luettich (2002), Lateral dynamic analysis and classification of barotropic tidal inlets, *Cont. Shelf Res.*, **22**, 2516–2631.
- Imasato, N. (1983), What is tide-induced residual current?, *J. Phys. Oceanogr.*, **13**, 1307–1317.
- Lu, Y., K. R. Thompson, and D. G. Wright (2001a), Tidal currents and mixing in the Gulf of St. Lawrence: An application of the incremental approach to data assimilation, *Can. J. Fish. Aquat. Sci.*, **58**, 723–735.
- Lu, Y., D. G. Wright, and D. Brickman (2001b), Internal tide generation over topography: Experiments with a free-surface z-level ocean model, *J. Atmos. Oceanic Technol.*, **18**, 1076–1091.
- Nihoul, J. C. J., and F. C. Ronday (1975), The influence of the "tidal stress" on the residual circulation—Application to the Southern Bight of the North Sea, *Tellus*, **27**, 484–489.
- Parker, B. B. (1991), The relative importance of the various nonlinear mechanisms in a wide range of tidal interactions (review), in *Tidal Hydrodynamics*, edited by B. B. Parker, pp. 237–268, John Wiley, Hoboken, N. J.
- Pawlowicz, R., B. Beardsley, and S. Lentz (2002), Classical tidal harmonic analysis including error estimates in MATLAB using T_TIDE, *Comput. Geosci.*, **28**, 929–937.
- Ridderinkhof, H., and J. T. F. Zimmerman (1990), Residual currents in the western Dutch Wadden Sea, in *Residual Currents and Long-Term Transport*, edited by R. T. Cheng, pp. 93–104, Springer-Verlag, New York.
- Robinson, I. S. (1981), Tidal vorticity and residual circulation, *Deep Sea Res.*, Part A, **28**, 195–212.
- Safer, A. (2002), MEPS: A prototype for the study of coastal dynamics, *Sea Technology*, **40**, 10–14.
- Sheng, J. (2001), Dynamics of a buoyancy-driven coastal jet: The Gaspé Current, *J. Phys. Oceanogr.*, **31**, 3146–3163.
- Sheng, J., and L. Tang (2003), A numerical study of circulation in the western Caribbean Sea, *J. Phys. Oceanogr.*, **33**, 2049–2069.
- Sheng, J., and L. Tang (2004), A two-way nested-grid ocean circulation model for the Meso-American Barrier Reef System, *Ocean Dyn.*, **54**, 232–242, doi:10.1007/s10236-003-0074-3.
- Sheng, J., D. G. Wright, R. J. Greatbatch, and D. E. Dietrich (1998), CANDIE: A new version of the DieCAST ocean circulation model, *J. Atmos. Oceanic Technol.*, **15**, 1414–1432.
- Sheng, J., R. J. Greatbatch, and D. G. Wright (2001), Improving the utility of ocean circulation models through adjustment of the momentum balance, *J. Geophys. Res.*, **106**, 16,711–19,728.
- Signell, R. P., and B. Butman (1992), Modeling tidal exchange and dispersion in Boston Harbor, *J. Geophys. Res.*, **97**, 15,591–15,606.
- Stommel, H., and H. G. Farmer (1952), On the nature of estuarine circulation, part I, *Woods Hole Oceanogr. Inst. Tech. Rep. 52-88*, 131 pp., Woods Hole, Mass.
- Sturley, D. R. M., and A. J. Bowen (1996), A model for contaminant transport in Lunenburg Bay, Nova Scotia, *Sci. Total Environ.*, **179**, 161–172.
- Sturley, D. R. M., K. R. Thompson, and A. J. Bowen (1993), Fine-scale models of coastal inlets: A physical basis for water quality/biological models, *Can. Coastal Conf. Proc.*, **1**, 387–398.
- Tee, K. T. (1976), Tide-induced residual current, a 2-D nonlinear numerical tidal model, *J. Mar. Res.*, **34**, 603–628.
- Tee, K. T. (1981), The structure of three-dimensional tidal-induced current, part II: Residual currents, *J. Phys. Oceanogr.*, **10**, 2035–2057.
- Thompson, K. R., and J. Sheng (1997), Subtidal circulation on the Scotian Shelf: Assessing the hindcast skill of a linear, barotropic model, *J. Geophys. Res.*, **102**, 24,987–25,003.
- Thompson, K. R., D. E. Kelley, D. Sturley, B. Topliss, and R. Leal (1998), Nearshore circulation and synthetic aperture radar: An exploratory study, *Int. J. Remote Sens.*, **19**, 1161–1178.
- Thurnburn, J. (1996), Multidimensional flux-limited advection schemes, *J. Comput. Phys.*, **123**, 74–83.
- Zimmerman, J. T. F. (1978), Topographic generation of residual circulation by oscillatory (tidal) currents, *Geophys. Astrophys. Fluid Dyn.*, **11**, 35–47.

J. Sheng and L. Wang, Department of Oceanography, Dalhousie University, Halifax, Nova Scotia, Canada B3H 4J1. (sheng@phys.ocean.dal.ca)